01 Jan 2023

An Extended Generalized Average Modeling Framework For Power Converters

Kartikeya Jayadurga Prasad Veeramraju

Jacob A. Mueller

Jonathan W. Kimball
Missouri University of Science and Technology, kimballjw@mst.edu

Recommended Citation

K. J. Prasad Veeramraju et al., "An Extended Generalized Average Modeling Framework For Power Converters," *IEEE Transactions on Power Electronics*, Institute of Electrical and Electronics Engineers, Jan 2023.
The definitive version is available at https://doi.org/10.1109/TPEL.2023.3276631

An Extended Generalized Average Modeling Framework for Power Converters

Kartikeya Jayadurga Prasad Veeramraju, *Student Member, IEEE,* Jacob A. Mueller, *Member, IEEE,* and Jonathan W. Kimball, *Senior Member, IEEE*

***Abstract*—The Generalized Averaged Modeling (GAM) technique is traditionally employed to capture the dynamic performance of power electronic converters. This paper proposes an improved version of it, named the Extended-GAM (EGAM) technique, which supports the multiplication of two Double Fourier Series (DFS) signals in the time domain. Multiplication of DFS signals in the time domain translates to the 2D-convolution of coefficients of the DFS terms of their equivalent Discrete Fourier Image (DFI) representations. Thus, the proposed EGAM technique, capable of capturing many harmonics present in the output of a power converter, effectively captures the dynamic behavior of power converters excited by two distinct frequencies. The proposed technique is then converted into an algorithm suitable for numerical platforms, which typically use Ordinary Differential Equation (ODE) solvers. The proposed algorithm is validated based on the observations of the effects of harmonic truncation. The efficacy of the proposed technique is assessed through a case study, wherein a single-phase inverter employs LC filters on both the dc-link and the ac-side. Finally, it is shown that the results obtained with the proposed method show an excellent congruence between simulation and hardware experimental models. Additionally, the proposed algorithm is packaged into a MATLAB toolbox and shared for future implementations.**

***Index Terms*—Generalized Averaged Models, Multi Frequency Averaging, Dynamic Phasor Modeling, Power Electronic Converters, Inverters.**

I. Introduction

THE Generalized Averaged Modeling (GAM) technique is instrumental in systems where Small Ripple Approximation (SRA) may not be applied, such as series-resonant converters, three-phase inverters, Dual Active Bridge (DAB) converters. Modeling poses difficulties, as the SRA about an operating point cannot be applied to such systems. The idea of GAM is first presented in [1], where selective frequencies for modeling various power electronic converters and operators over a state variable expressed as Fourier coefficients were presented. GAM is applied to a dc-dc converter, and its frequency-dependent structure is described [1]–[3]. The product of two Fourier coefficients for the dc and fundamental terms is shown [1], [2]. These product terms are directly used in subsequent works using GAM treatment on DABs [4]–[7], series resonant converters [8], Modular Multilevel Converter (MMC) [9], [10], and microgrids [11]. Of late, GAM is also being referred to as the *Dynamic Phasor Modeling* (DPM) technique as described in the works on inverter modeling studies [12]–[14], and diode bridge rectifiers [15]. GAM was also shown to model and describe the stability behavior of inverter-based microgrids by eigenvalue analysis [16] for imbalance conditions and advanced droop control techniques [17]. It is shown in [18] that, unlike other models, the GAM technique can capture multi-frequency dynamics in conventional dc-dc converters. A *dimension* in the context of this work refers to an excitation frequency. Therefore, a GAM technique using a single frequency is called uni-dimensional GAM.

The necessity for including two excitation frequencies must be concretely set to realize the motivation for this work. Fig. 1 shows models of increasing complexity, introduced alongside exemplary topologies, connecting each increase in model complexity to a different specific modeling requirement. A buck converter is shown in Fig. 1(a). This converter is assumed to have the ripple value Δx in its state variables that is much smaller than the dc component x_{dc} (i.e., $\Delta x \ll x_{\mathrm{dc}}$). Therefore, State Space Averaging (SSA) technique has traditionally been applied to capture the dynamics of the inductor current and the capacitor voltage. The SSA technique cannot be used where switching level dynamics cannot be ignored. The GAM technique is effective in such an application space, which captures the switching level dynamics [2].

As a next example, a Dual Active Bridge (DAB) converter is shown in Fig. 1(b). In this situation, the SSA fails to capture the inductor dynamics as the inductor current waveform (shown in the figure) has a zero dc value and a highly dominant switching frequency component (thus SRA fails too). Therefore, the GAM technique is needed to model the behavior of the leakage inductance dynamics of DAB [4], [19].

A single frequency of excitation is considered in the works described thus far. These frameworks are extended to the second dimension in the works described in the following paragraphs. Inverters and ac-ac converters [20]–[22] have two excitation frequencies, namely, the switching frequency and the modulation frequency. In such a scenario, a uni-dimensional GAM framework cannot support capturing the two frequency components in the system. For example, a single-phase inverter schematic is shown in Fig. 1(c). The modulation and switching frequencies are injected into the inverter via the switching signals, and the inverter fabricates the modulation frequency and the subsequent odd harmonics. The switching ripple rides on top of this signal as well. Therefore, the inverter's dynamic model has four frequency categories: the dc, switching frequency, modulation frequency, and sideband components. To facilitate the capturing of these

KJP. Veeramraju and J. Kimball are with the Department of Electrical and Computer Engineering, Missouri University of Science and Technology, Rolla, MO, 65401 USA e-mail: kvkhh@mst.edu, kimballjw@mst.edu.

J. A. Mueller is with Sandia National Laboratories, Albuquerque, NM, 87185 USA.

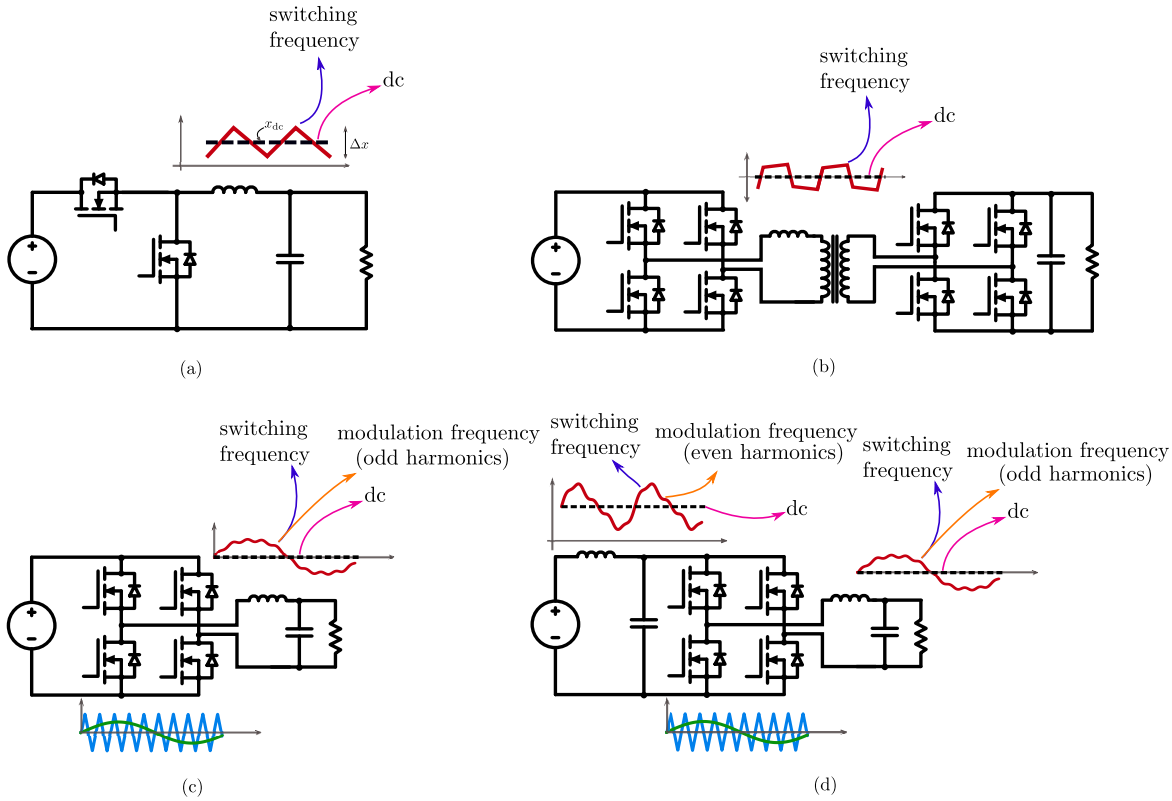

Fig. 1: Various power converters: (a) a buck converter with single switching frequency; SSA applicable, (b) a DAB converter with single switching frequency; SSA not applicable, (c) an inverter with SPWM with two distinct frequencies of excitation, (d) an inverter with input LC filter, with two distinct frequencies of excitation

components, two frequencies are to be considered in the two-dimensional GAM (2D-GAM) framework [23]–[26].

Although the extension to the second dimension was made in the 2D-GAM framework [16], [23], it can be difficult to model all converter classes with two excitation frequencies with the existing literature. An inverter with an LC filter on the dc side is shown in Fig. 1(d) as an example topology. The state variables on the ac side have dc, modulation, and switching components that can be modeled in 2D-GAM. However, the dc side of the inverter possesses the dc, even order modulation harmonics, and the switching components. The Sine Pulse Width Modulation (SPWM) results in the spectral components shown in Fig. 2. The spectrum has three types of components: modulation frequency harmonics ($p\bar{f}$), switching frequency harmonics ($r\hat{f}$), and sideband components ($r\hat{f}+p\bar{f}$) where $p \in \mathbb{Z}$, and $r \in \mathbb{W}$. The magnitude of the switching signal is zero at modulation frequency harmonics above the fundamental, which makes them difficult to be considered in 2D-GAM. This paper proposes a novel 2D convolution-based Extended GAM (EGAM) framework, as harmonic components do not naturally manifest in the 2D-GAM framework, and it is difficult to keep track of the manifestations. The proposed framework accounts for the dynamics at the initially considered frequencies and newly manifesting frequencies of the system. Therefore, the main contributions of this work are to develop:

1) A consistent framework for handling the Single Fourier Series (SFS) or Double Fourier Series (DFS) products

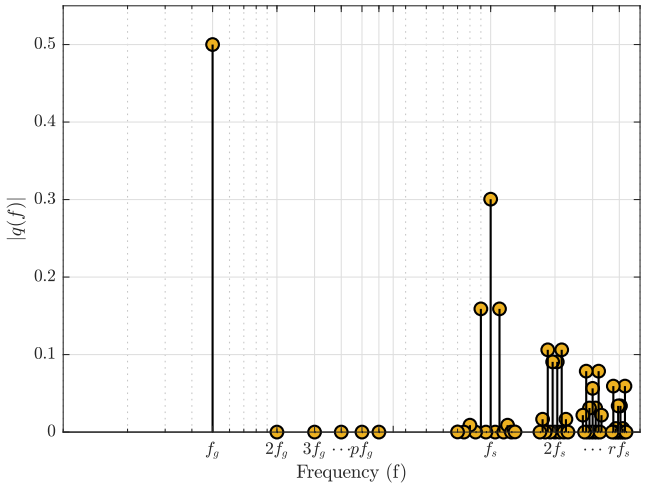

Fig. 2: Spectral components in SPWM switching waveform

2) An algorithm for handling 2D convolutions in frequency plane to enable EGAM in numerical ODE solvers

This article is organized as follows: a review of the conventional GAM technique is first presented in Section II. The idea of Discrete Fourier Images (DFI) is presented in Section III, succeeded by the Extended GAM modeling technique. The properties of harmonic truncation (a consequence of EGAM) are explored in Section IV. Hardware results for an example single phase inverter in Section V are presented to test the

model's efficacy, and the results are analyzed.

II. Review of GAM

In conventional GAM, the time-dependent state variables are transformed to the Fourier coefficients written as Single Fourier Series (SFS) expansions; that is, a periodic signal $x(t)$ in the time domain can be written as

$$x(t) = \sum_{k=-\infty}^{+\infty} x_k e^{jk\omega_0 t} \tag{1}$$

$$\mathbf{C}(t) = \begin{bmatrix} 1 & \cos(\bar{\omega}t) & \sin(\bar{\omega}t) & \cdots & \cos(n\bar{\omega}t) & \sin(n\bar{\omega}t) \end{bmatrix} \tag{2}$$

$$x(t) = \mathbf{C}(t) \cdot \mathbf{x}_k^{\intercal} \tag{3}$$

where $\mathbf{x}_k$ is the vector of Fourier coefficients

$$\mathbf{x}_k = \begin{bmatrix} x_0 & x_{1c} & x_{1s} & \cdots & x_{nc} & x_{ns} \end{bmatrix} \tag{4}$$

With these base relationships, the framework can be extended for other operators [1], [2], [24] given by

$$\frac{d}{dt}\langle x\rangle_k(t) = \left\langle \frac{d}{dt}x \right\rangle_k (t) - jk\omega_0 \langle x\rangle_k(t) \tag{5}$$

$$\langle xy\rangle_k = \sum_{i=-\infty}^{\infty} \langle x\rangle_{k-i}\langle y\rangle_i \tag{6}$$

the operator $\langle \bullet \rangle_k$ represents the k^{th} harmonic Fourier coefficient of a time domain signal and (6) is a discrete 1D convolution [27].

If the system of interest has two distinct excitation frequencies, namely ω_1, ω_2, the state variable $x(t)$ in the time domain is represented using DFS given by

$$x(t) = \sum_{p\in\mathbb{Z}, r\in\mathbb{W}} \mathrm{x}_{p,r} e^{i(p\omega_1 t + r\omega_2 t)} \tag{7}$$

then it can be converted to the vector containing the Fourier coefficients for a finite number of harmonics as

$$\mathbf{x} = \begin{bmatrix} \mathrm{x}_{0,0} & \mathrm{x}_{1,0c} & \mathrm{x}_{1,0s} & \cdots & \mathrm{x}_{0,1c} & \mathrm{x}_{0,1s} & \cdots & \mathrm{x}_{p,rc} & \mathrm{x}_{p,rs} \end{bmatrix} \tag{8}$$

where, $\mathrm{x}_{p,0c}$, $\mathrm{x}_{p,0s}$ belong to the Fourier coefficients of the harmonics of ω_1; $\mathrm{x}_{0,rc}$, $\mathrm{x}_{0,rs}$ belong to coefficients of the harmonics of ω_2, and $\mathrm{x}_{p,rc}$, $\mathrm{x}_{p,rs}$ belong to coefficients of the harmonics of $p\omega_1 + r\omega_2$ components. The subscripts c and s correspond to the cos and sin terms of the DFS expansion in rectangular form.

In order to extend the GAM framework to 2D-GAM, (5) is rewritten as

$$\frac{dx(t)}{dt} = \mathbf{C}(t)\left(\frac{d\mathbf{x}}{dt} + \mathbf{T}\mathbf{x}\right) \tag{9}$$

where the DFS coefficients of the expansion are stored in the state variable $\mathbf{x}$ (8) and the matrix $\mathbf{T}$ stores the frequency information at the state variable $\mathrm{x}_{p,r}$. Therefore, $\mathbf{T}$ is the matrix version of the second term of GAM (5) given by

$$\mathbf{T}_{(2k,2k+1)} = (\mathbf{m}_{k+1}\omega_1 + \mathbf{n}_{k+1}\omega_2) \tag{10}$$

$$\mathbf{T}_{(2k+1,2k)} = -(\mathbf{m}_{k+1}\omega_1 + \mathbf{n}_{k+1}\omega_2) \tag{11}$$

where $k \in \mathbb{N}^O$, indexes the vectors $\mathbf{m} \in \mathbb{Z}^{O+1}$,and $\mathbf{n} \in \mathbb{W}^{O+1}$. Dimensionally, $\mathbf{T}$ is a $(2O+1)\times(2O+1)$ sparse matrix [23]. O is the total number of distinct frequencies and harmonic combinations considered, excluding the dc term and $k \in \{1, 2, \cdots O\}$. Vectors $\mathbf{m}$ and $\mathbf{n}$ have an order of one more than the distinct frequencies (O) to account for the dc term, which is always the first entry from an indexing viewpoint. With these base equations, a first-order differential equation of the form

$$\frac{dx(t)}{dt} = ax(t) + by(t) \tag{12}$$

can be rewritten in the Fourier coefficients and using (3)

$$\left\langle \frac{dx(t)}{dt} \right\rangle = a\langle x(t)\rangle + b\langle y(t)\rangle \tag{13}$$

$$\frac{d\mathbf{x}}{dt} = (a\mathbf{I} - \mathbf{T})\mathbf{x} + b\mathbf{y} \tag{14}$$

where $\mathbf{x}$, $\mathbf{y}$ are Fourier coefficient vectors at the same frequencies. Applying the same procedure on a more complicated base first-order ordinary differential equation

$$\frac{dx(t)}{dt} = ax(t) + bx(t)y(t) \tag{15}$$

$$\frac{d\mathbf{x}}{dt} = (a\mathbf{I} - \mathbf{T})\mathbf{x} + b(\mathbf{x} * \mathbf{y}[\ell]) \tag{16}$$

Eq. (16) can then be expanded for the desired number of harmonics (by writing for each harmonic order, $\ell \in (1, 2, \cdots, O)$) to finally give

$$\begin{aligned} \frac{d}{dt}\begin{bmatrix} x_0 \\ x_{1c} \\ x_{1s} \\ \vdots \\ x_{lc} \\ x_{ls} \end{bmatrix} &= \begin{bmatrix} a & 0 & 0 & 0 & \cdots & 0 \\ 0 & a & -\omega_1 & 0 & \cdots & 0 \\ 0 & \omega_1 & a & 0 & \cdots & 0 \\ \vdots & \vdots & \vdots & \ddots & \vdots & \vdots \\ 0 & 0 & 0 & 0 & a & -\omega_l \\ 0 & 0 & 0 & 0 & \omega_l & a \end{bmatrix}\begin{bmatrix} x_0 \\ x_{1c} \\ x_{1s} \\ \vdots \\ x_{lc} \\ x_{ls} \end{bmatrix} \\ &+ b\begin{bmatrix} \sum_{u=-\infty}^{\infty} x[u]y[-u] \\ \Re\left\{\sum_{u=-\infty}^{\infty} x[u]y[1-u]\right\} \\ \Im\left\{\sum_{u=-\infty}^{\infty} x[u]y[1-u]\right\} \\ \vdots \\ \Re\left\{\sum_{u=-\infty}^{\infty} x[u]y[l-u]\right\} \\ \Im\left\{\sum_{u=-\infty}^{\infty} x[u]y[l-u]\right\} \end{bmatrix} \end{aligned} \tag{17}$$

In (15), the product of two SFS terms, $x(t)y(t)$, translated to 1D discrete convolution on the frequency plane for the Fourier coefficient vectors $\mathbf{x}$, $\mathbf{y}$ [1], [2], [25], [26], [28]. The translation from the time domain to the frequency domain for the multiplication of two terms expressed as DFS is not reported in the literature. Although [26] considered a three-phase inverter with an input LC filter, the article only considers the existing spectral components in the SPWM waveform and does not accommodate newly manifesting harmonics. Also, [29] notes that the multiplication of two DFS terms must be considered in the future and points out that the authors did not view the product terms in their work. This crucial result is needed to accurately capture the dynamic performance of many power electronic converters, where a switching term multiplies over a state variable, as in the case of an inverter with an LC filter on the dc side. Although more recent work in microgrids [16] considers dc filter dynamics,

it does not explain how similar relationships are derived for other harmonics in an organized way. The following section discusses the process of handling the product of two DFS terms and lays the foundation for EGAM.

III. Extended GAM with Discrete Fourier Images

In a one-dimensional case, the product of two state vectors consisting of coefficients in the time domain will imply convolution in the frequency domain [27], a direct consequence of the convolution theorem. A corollary can be stated in this regard,

Corollary 3.0.1: *The product of two sinusoidal signals of the same period produces a waveform with Fourier coefficients matching the discrete convolution of the original signals in the frequency domain.*

Most works listed so far only consider a select number of terms to compute the product terms while neglecting the others. When multiple fundamental frequencies of operation are considered, as in an inverter, the convolution operator becomes very complicated, and a concrete methodical way of resolving the products must be devised.

To handle the product terms, a two-dimensional extension can be made to the already existing Corollary 3.0.1 and can be restated as,

Corollary 3.0.2:

The product of two sinusoidal signals, with two distinct periods, produces a waveform with Fourier coefficients matching the two-dimensional discrete convolution of the original signals in the frequency domain.

Based on corollary 3.0.2, the frequency component vectors must be convolved over two dimensions to obtain the resulting component vector. However, the Fourier vector must be transformed to a discrete frequency plane, where the Fourier components must be placed before the 2D convolution is applied. Proof for Corollary 3.0.2 is provided in Appendix A. The following subsections describe a methodical way to place and keep track of new harmonics when there are two distinct excitation frequencies.

A. Discrete Fourier Image signal

The vector $\mathbf{x}$ (8) can be separated into two new vectors consisting of the coefficients of c and s subscripts to give

$$\begin{aligned}\mathbf{a} &= \begin{bmatrix} x_{0,0} & x_{1,0c} & \cdots & x_{0,1c} & \cdots & x_{p,rc} \end{bmatrix} \\ \mathbf{b} &= \begin{bmatrix} 0 & x_{1,0s} & \cdots & x_{0,1s} & \cdots & x_{p,rs} \end{bmatrix}\end{aligned} \tag{18}$$

where the dc term is accounted into the c vector term and the corresponding value in $\mathbf{b}$ is left to zero. The vectors (18) can then be converted to complex notation for each harmonic index given using the transformation

$$\begin{aligned}\alpha_{p,r} &= \begin{cases} a_0, \text{for } p=0, r=0 \\ \frac{1}{2}(a_g - \mathrm{i}b_g), \text{ otherwise} \end{cases} \\ \alpha^*_{(p,r)} &= \frac{1}{2}(a_g + \mathrm{i}b_g)\end{aligned} \tag{19}$$

The subscripts of each element of $\mathbf{a}$, $\mathbf{b}$ ($x_{\bullet,\bullet}$) indexed by $g \in \mathbb{N}$ get carried over to the subscripts of $\alpha_{\bullet,\bullet}$, and $\alpha^*_{\bullet,\bullet}$. The calculated components can then be placed on an image space to represent a 2D signal corresponding to the Fourier coefficients at the discrete instances of the harmonic numbers as shown in Fig. 3. As the two frequencies of the signal are distinct, each Fourier coefficient can be placed in a distinct location on the 2D image plane formed by ω_1 and ω_2 axes. This forms the basis for the rest of the discussion in this article.

A matrix can then be generated based on Fig. 3 and is given by

$$\mathbf{F} = \begin{bmatrix} \alpha_{-p,r} & \cdots & \alpha_{-1,r} & \alpha_{0,r} & \alpha_{1,r} & \cdots & \alpha_{p,r} \\ \vdots & \ddots & \ddots & \vdots & \iddots & \iddots & \vdots \\ \alpha_{-p,1} & \ddots & \alpha_{-1,1} & \alpha_{0,1} & \alpha_{1,1} & \iddots & \alpha_{p,1} \\ \alpha^*_{p,0} & \cdots & \alpha^*_{1,0} & \alpha_{0,0} & \alpha_{1,0} & \cdots & \alpha_{p,0} \\ \alpha^*_{p,1} & \iddots & \alpha^*_{1,1} & \alpha^*_{0,1} & \alpha^*_{-1,1} & \ddots & \alpha^*_{-p,1} \\ \vdots & \iddots & \iddots & \vdots & \ddots & \ddots & \vdots \\ \alpha^*_{p,r} & \cdots & \alpha^*_{1,r} & \alpha^*_{0,r} & \alpha^*_{-1,r} & \cdots & \alpha^*_{-p,r} \end{bmatrix} \tag{20}$$

where $\mathbf{F}$ is referred to as the *Discrete Fourier Image* (DFI) [30] of Fourier coefficient vector $\mathbf{x}$. The DFI has nine regions, differentiated by different symbols, as seen in the DFI image shown in Fig. 3. A legend for each symbol corresponding to each harmonic component with their p and r axis values is given in Table I

Now, using Corollary 3.0.2, two Fourier coefficient vectors $\mathbf{x}$, and $\mathbf{y}$ can be 2D convolved to get a larger matrix. These relations are mathematically given by

$$x(t) \xleftrightarrow{\mathcal{F}} \mathbf{x} \xleftrightarrow{\text{DFI}} \mathbf{F_x} \tag{21}$$

$$y(t) \xleftrightarrow{\mathcal{F}} \mathbf{y} \xleftrightarrow{\text{DFI}} \mathbf{F_y} \tag{22}$$

$$z(t) \xleftrightarrow{\mathcal{F}} \mathbf{z} \xleftrightarrow{\text{DFI}} \mathbf{F_z} \tag{23}$$

$$z(t) = x(t)y(t) \xleftrightarrow{\text{DFI}} \mathbf{F_z} = \mathbf{F_x} ** \mathbf{F_y} \tag{24}$$

where $\mathcal{F}$ is the Fourier series coefficient extraction operation from the time domain signal $\bullet(t)$. The resulting matrix $\mathbf{F}_z$ is converted back to the vector $\mathbf{z}$ by using the transformation

$$\begin{aligned} h_g &= \begin{cases} \alpha_{0,0}, \text{for } p=0, r=0 \\ \alpha_{p,r} + \alpha^*_{p,r} \text{ otherwise} \end{cases} \\ s_g &= \mathrm{i}(\alpha_{p,r} - \alpha^*_{p,r}) \end{aligned} \tag{25}$$

The resulting values are populated in $\mathbf{h}$, $\mathbf{s}$ and redistributed in the proper harmonic order as that of (8) to form the vector $\mathbf{z}$, which is the resulting vector of the 2D convolution.

Before proceeding with the subsequent sections, an essential distinction between convolution operators should be made. The 2D convolution and Corollary 3.0.2 are applied when the vector is converted to DFI as shown in Fig. 3. Therefore, to simplify the notation, for vectors $\mathbf{x}$, and $\mathbf{y}$, a new notation $\mathbf{x} \circledast \circledast \mathbf{y}$ is defined to mean $\mathbf{z}$, which is converted using (25) on $\mathbf{F_x} ** \mathbf{F_y}$. That is, $\circledast \circledast$ represents the complete process

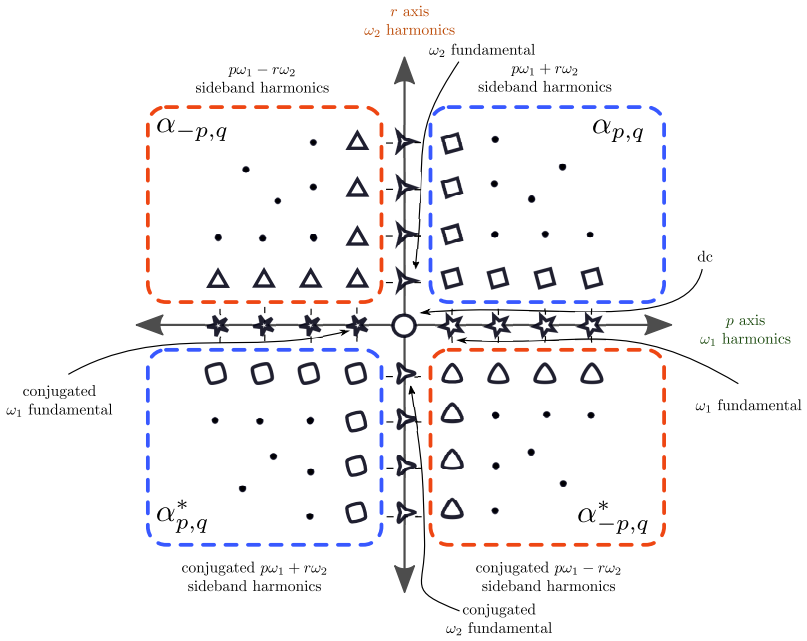

Fig. 3: Two dimensional DFI signal representation

TABLE I: Legend for DFI components in Fig. 3

Component	Axis	Symbol
dc component	$p = 0; r = 0$	
ω_1 harmonics	$p \in \mathbb{Z}^+; r = 0$	
ω_2 harmonics	$p = 0; r \in \mathbb{Z}^+$	
ω_1, ω_2 sidebands	$p \in \mathbb{Z}^+; r \in \mathbb{Z}^+$	
$-\omega_1, \omega_2$ sidebands	$p \in \mathbb{Z}^-; r \in \mathbb{Z}^+$	
ω_1 harmonics' conjugates	$p \in \mathbb{Z}^+; r = 0$	
ω_2 harmonics' conjugates	$p = 0; r \in \mathbb{Z}^+$	
ω_1, ω_2 sidebands' conjugates	$p \in \mathbb{Z}^+; r \in \mathbb{Z}^+$	
$-\omega_1, \omega_2$ sidebands' conjugates	$p \in \mathbb{Z}^-; r \in \mathbb{Z}^+$	

of rectangular to complex DFI to double convolution and back to rectangular form.

For systems excited by two different base fundamental frequencies, such as in the case of an inverter, the vector $\mathbf{x}$ is extended to capture multiple baseband harmonics and the sidebands harmonics by their respective DFS expansions. However, in [23], [24], the expansion for the product of two state vectors written as DFS is not provided as indicated earlier in Section II. Also, the authors make simplifying assumptions to avoid the multiplication terms by neglecting state variables that multiply with a switching term by choosing simpler topologies. In [25], [26], however, the dc side filters in the inverter are modeled. The authors consider only a few harmonics in their 2D-GAM model and do not consider even harmonics of the modulation signal.

Referring back to (15), and assuming $x(t)$ and $y(t)$ to be DFS expansions instead of SFS, (16) can be expanded into the second dimension by

$$\frac{d\mathbf{x}}{dt} = (a\mathbf{I} - \mathbf{T})\mathbf{x} + b(\mathbf{x} \circledast \circledast \mathbf{y}) \tag{26}$$

This completes the EGAM formulation that is capable of handling DFS products. A complete set of the time domain to EGAM translations is shown in Table II for clarity. The following subsection shows an algorithm for handling DFS products in Ordinary Differential Equation (ODE) solvers for making EGAM implementable with the MATLAB simulation software package.

TABLE II: EGAM operations set

Operation	Time Domain	Frequency Domain
Scalar Product	$ax(t)$	$a\mathbf{x}$
Summation	$x(t) + y(t)$	$\mathbf{x} + \mathbf{y}$
Differentiation	$\frac{dx(t)}{dt}$	$\left(\frac{d\mathbf{x}}{dt} + \mathbf{T}\mathbf{x}\right)$
Multiplication	$x(t)y(t)$	$\mathbf{x} \circledast \circledast \mathbf{y}$

B. Convolution Algorithm for ODE Solvers

An algorithm is proposed for computing the 2D convolution of the Fourier image signals in each processing cycle of a numerical ODE solver.

A step-by-step process for the DFI convolution algorithm is shown in Fig. 4. In the first step, the vectors $\mathbf{x}$ and $\mathbf{y}$ are first imported from the ODE process call. The imported vectors are then split into real and imaginary component vectors shown by the subscripts $\mathbb{R}$, $\mathbb{I}$ in the second step. The split vectors are transformed into the corresponding DFI in the third step. In the fourth step, the 2D convolution operator is applied to the two DFIs, and the resultant DFI is shown. The size of the resulting matrix is larger than both of the individual input matrices. Therefore, to restrict the length of the resultant vector, the new harmonics cropping up are neglected in the fifth step to prevent the growth of vectors as the ODE solver progresses. This method of ignoring harmonic components beyond the allowed size of the input vectors is referred to as *harmonic truncation*. The effects of making the harmonic truncation approximation will be studied in further detail in the next section. The truncated DFI is transformed into the real

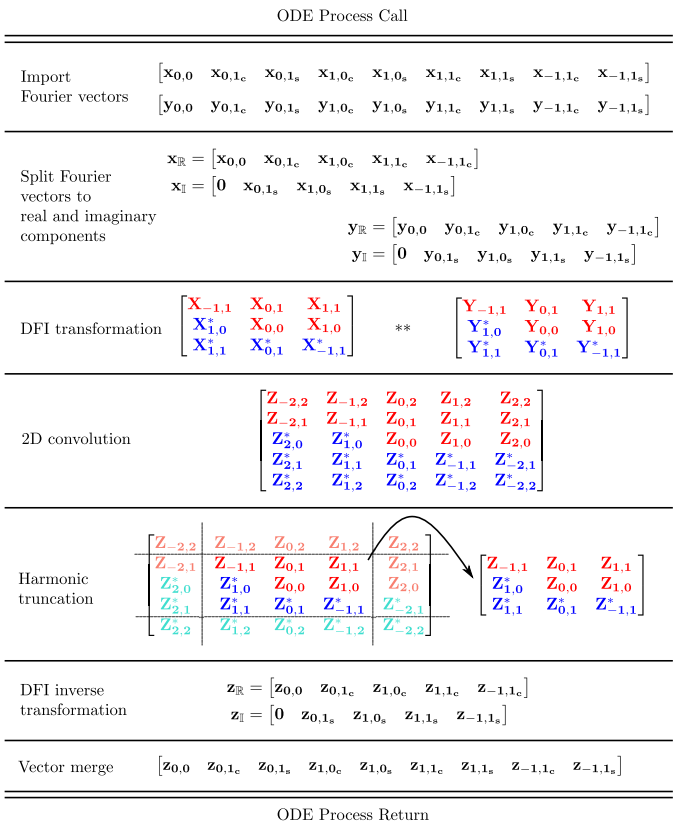

Fig. 4: Proposed convolution algorithm for resolving $z = \mathbf{x} \circledast \circledast \mathbf{y}$ in an ODE solver

and imaginary component vectors, merged into one contiguous vector in the last step, and handed over to the ODE process. A MATLAB toolbox is developed for systematically performing the 2D convolution computations and is shared publicly as a GitHub project in Appendix B to aid future implementations.

IV. Harmonic Truncation

When two DFI signals are convolved, the size of the resulting DFI ($\mathbf{F_z}$) increases indicating the evolution of new harmonic components. However, if the size of the DFI increases, it will also increase the resulting Fourier coefficient vector length and will impose further requirements on the memory allocation aspects in the ODE solver front. To alleviate this issue, harmonic truncation is necessary to restrict the growth of the size of the $\mathbf{F_z}$ matrix. However, the harmonic truncation approximation may not be a viable technique always as it depends on the relative scales of amplitudes of the DFI signals. Two examples are provided in this section: one where the process of harmonic truncation shows a detrimental behavior and the other where it is a reasonable approximation.

A. Detrimental effects of harmonic truncation

Consider $x(t)$ and $y(t)$ to be two input signals as functions of ω_1 and ω_2, given by

$$x(t) = 150\cos(\omega_1 t) - 1.5\cos(\omega_2 t) + 2.5\cos(\omega_1 t + \omega_2 t) + 10\cos(-\omega_1 t + \omega_2 t) - 1.75\sin(-\omega_1 t + \omega_2 t) \quad (27)$$

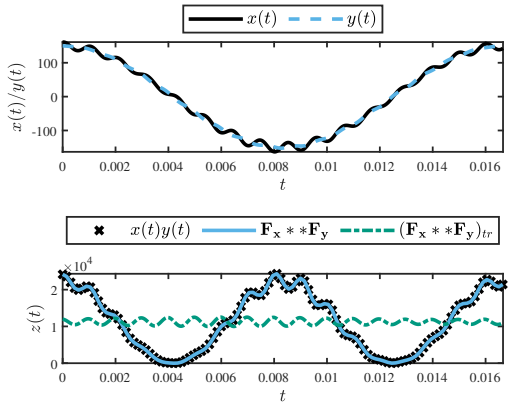

Fig. 5: Detrimental effects of harmonic truncation; p axis restricted to fundamental harmonic

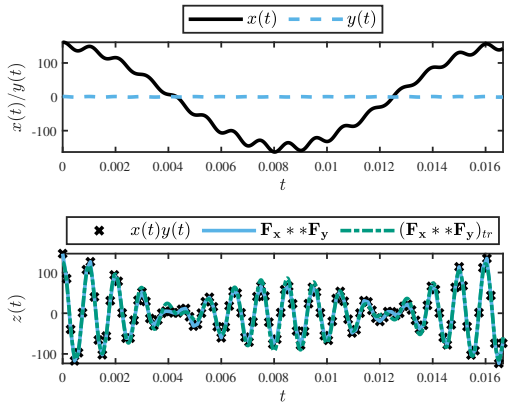

Fig. 6: Good approximation by harmonic truncation; p axis restricted to fundamental harmonic

$$y(t) = 150\cos(\omega_1 t) + 1.5\sin(\omega_2 t) - 1.5\sin(\omega_1 t + \omega_2 t) + 0.75\sin(-\omega_1 t + \omega_2 t) \quad (28)$$

Fig. 5 shows the two input signals described in (27) and (28) and the actual product $z(t) = x(t)y(t)$. Also shown are the truncated and un-truncated time domain reconstructions of the two DFI signals represented by $\mathbf{F}_{\mathbf{z}tr} = (\mathbf{F_x} ** \mathbf{F_y})_{tr}$ and $\mathbf{F_z} = \mathbf{F_x} ** \mathbf{F_y}$ respectively. The two signals (27), (28) have a dominant ω_1 component, and their product will have a dominant $2\omega_1$ component. To capture the second-order components, the DFI needs to be extended by an extra harmonic order on the p (ω_1) axis, which is one order higher than the original sizes of the input DFIs $\mathbf{F_x}$, and $\mathbf{F_y}$. If this harmonic order extension is not done, the crucial $2\omega_1$ feature of the resulting product signal $z(t)_{tr}$ will be lost and the truncated 2D convolution of the DFI leads to a drastically different result when compared to the case where the $2\omega_1$ components are considered (as indicated by the untruncated DFI reconstruction in Fig. 5).

B. Good harmonic truncation

In this example, two signals are again selected, where the first operator $x(t)$ is the same as in (27). But $y(t)$ is replaced

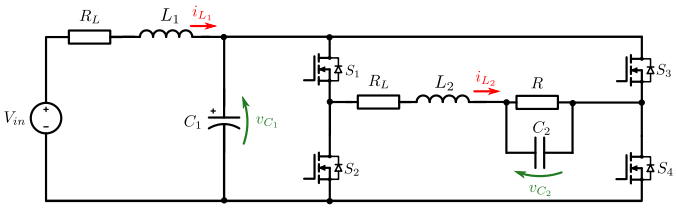

Fig. 7: Single phase inverter

with

$$y(t) = 0.01\cos(\omega_1 t) + 0.7\cos(\omega_2 t) + 0.1\cos(\omega_1 t + \omega_2 t) + 0.1\cos(-\omega_1 t + \omega_2 t) \tag{29}$$

Fig. 6 shows the two input signals described in (27) and (29) and the actual product $z(t) = x(t)y(t)$. This case however shows a close match between $z(t)$ and the reconstructions of $\mathbf{F_z}$, and $\mathbf{F}_{\mathbf{z}tr}$ DFIs. The close match is attributed to non-dominant $2\omega_1$ components due to the high order difference between the Fourier coefficients of the ω_1 components of $x(t)$ and $y(t)$.

This shows that essential features of the product signals can be lost if dominant harmonics lie outside the region of harmonic order approximation. Therefore, the system designer must know the entire range of dominant harmonics before deciding on the truncation region in EGAM. If dominant harmonics are neglected, the dynamic behavior of the model will be significantly different from the actual detailed/hardware model.

V. Experimental Validation

A single-phase inverter is used to test the validity of the DFI convolution algorithm. A schematic of the inverter is shown in Fig. 7. The inverter has an input LC filter to filter the input current ripple and an LC-filtered output for the load resistance R. The input filter has an inductor L_1, capacitor C_1, and the output filter has an inductor L_2, capacitor C_2. The series resistance of both the filter inductors, R_L, is assumed to be the same.

A. Formation of EGAM model for single-phase inverter

Based on the schematic, four state equations can be written for the converter in the time domain for the dynamic elements L_1, C_1, L_2, and C_2 having state variables i_{L_1}, v_{C_1}, i_{L_2}, and v_{C_2} which are given by

$$\begin{aligned}
\frac{di_{L_1}(t)}{dt} &= -\frac{R_L}{L_1} i_{L_1}(t) - \frac{v_{C_1}(t)}{L_1} + \frac{V_{in}}{L_1} \\
\frac{dv_{C_1}(t)}{dt} &= \frac{i_{L_1}(t)}{C_1} - \frac{i_{L_2}(t)}{C_1}(q_+(t) - q_-(t)) \\
\frac{di_{L_2}(t)}{dt} &= \frac{v_{C_1}(t)}{L_2}(q_+(t) - q_-(t)) - \frac{R_L}{L_2} i_{L_2}(t) - \frac{v_{C_2}(t)}{L_2} \\
\frac{dv_{C_2}(t)}{dt} &= \frac{i_{L_2}(t)}{C_2} - \frac{v_{C_2}(t)}{RC_2}
\end{aligned} \tag{30}$$

In (30) $q_+(t)$, and $q_-(t)$ are the switching functions originating from the SPWM of the H-bridge. In the switching expression, the symbols $\bar{f}$ and $\hat{f}$ represent the modulation frequency and the switching frequency respectively. Similarly, the symbols, p, and r denote the harmonic indices of $\bar{f}$, and $\hat{f}$. The DFS expansion consists of the modulation frequency and its harmonics (i.e., $p\bar{f}$), switching frequency, and its harmonics (i.e., $r\hat{f}$).

The DFS expansion for the SPWM signal is presented in (31), wherein the coefficients $q_{p,r}$ are provided in [23], which are repeated in (32).

$$q(t) = \sum_{p,r\in\mathbb{Z}} q_{p,r} e^{i(p\omega_1 t + r\omega_2 t)} \tag{31}$$

$$\begin{aligned}
q_{0,0} &= \frac{1}{2} \\
q_{1,0c} &= \frac{1}{2} m_{1,0c} \\
q_{1,0s} &= \frac{1}{2} m_{1,0s} \\
q_{p,rc} &= \frac{2}{p\pi} \sin\left(\frac{\pi(p+q)}{2}\right) J_p(y_r) \cos(p\bar{\phi} + r\hat{\phi}) \\
q_{p,rs} &= -\frac{2}{p\pi} \sin\left(\frac{\pi(p+q)}{2}\right) J_p(y_r) \sin(p\bar{\phi} + r\hat{\phi}) \\
y_x &= \frac{x\pi}{2}\sqrt{m_{1,0c}^2 + m_{1,0s}^2} \\
\bar{\phi} &= \arg(m_{1,0c} - j m_{1,0s}) \\
m_{1,0} &= \sqrt{m_{1,0c}^2 + m_{1,0s}^2}
\end{aligned} \tag{32}$$

$q_{0,0}$, $q_{1,0c/s}$ are the dc and modulation frequency components of the SPWM signal. $m_{1,0c}$, $m_{1,0s}$ are the cos and sin projections of the modulation index $m_{1,0}$ along the angle $\bar{\phi}$, which is the phase of the modulation signal. The cos and sin coefficients of switching frequency and sideband components of the switching signal are computed in $q_{p,rc}$, and $q_{p,rs}$, respectively. $J_\bullet(\bullet)$ is the Bessel function of the first kind.

Now, the time domain equations for the inverter system in (30) are rewritten in the frequency domain using the already existing relation (9) for derivatives and the newly proposed DFI convolution equation in (24) for products yield

$$\frac{d\mathbf{i}_{L_1}}{dt} = -\left(\frac{R_L}{L_1}\mathbf{I} + \mathbf{T}\right)\mathbf{i}_{L_1} - \frac{1}{L_1}\mathbf{v}_{C_1} + \frac{V_{in}}{L_1}\mathbf{\Gamma} \tag{33}$$

$$\frac{d\mathbf{v}_{C_1}}{dt} = \frac{1}{C_1}\mathbf{i}_{L_1} - \frac{1}{C_1}(2\mathbf{i}_{L_2} \circledast\circledast \mathbf{q}_+ - \mathbf{i}_{L_2} \circledast\circledast \mathbf{\Gamma}) - \mathbf{T}\mathbf{v}_{C_1} \tag{34}$$

$$\begin{aligned}
\frac{d\mathbf{i}_{L_2}}{dt} = &\frac{1}{L_2}(2\mathbf{v}_{C_1} \circledast\circledast \mathbf{q}_+ - \mathbf{v}_{C_1} \circledast\circledast \mathbf{\Gamma}) \\
&- \left(\frac{R_L}{L_2}\mathbf{I} + \mathbf{T}\right)\mathbf{i}_{L_2} - \frac{1}{L_2}\mathbf{v}_{C_2}
\end{aligned} \tag{35}$$

$$\frac{d\mathbf{v}_{C_2}}{dt} = \frac{\mathbf{i}_{L_2}}{C_2} - \left(\frac{1}{RC_2}\mathbf{I} + \mathbf{T}\right)\mathbf{v}_{C_2} \tag{36}$$

where $\mathbf{\Gamma} = \begin{bmatrix}1 & 0 & 0 & \cdots & 0\end{bmatrix}^{\mathrm{T}}$ and $\mathbf{I}$ is the identity matrix. As the input voltage V_{in} is dc, it only operates over the dc terms. Also, the switching terms $\mathbf{q}_+$ and $\mathbf{q}_-$

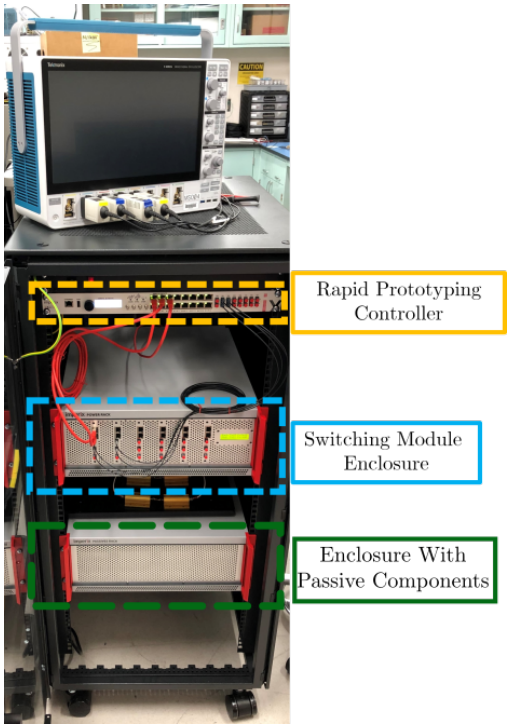

Fig. 8: Imperix system setup for a single phase inverter experimentation

are complementary and therefore, $(\mathbf{q}_+ - \mathbf{q}_-)$ is replaced by $(2\mathbf{q}_+ - \mathbf{\Gamma})$ [23].

As the inverter has both an input and an output filter, even harmonics of the modulation frequency are also to be considered for accurately capturing the dynamics of L_1 and C_1. In this work, one switching harmonic, and four modulation harmonics are considered, resulting in the Fourier vectors for each state $\mathbf{x}$.

$$\mathbf{x} = [x_{0,0},\ x_{1,0c},\ x_{1,0s}\ x_{2,0c},\ x_{2,0s},\ x_{3,0c},\ x_{3,0s}\ x_{4,0c},\ x_{4,0s}\ x_{1,1c},\ x_{1,1s}\ x_{-1,1c},\ x_{-1,1s}\ x_{2,1c},\ x_{2,1s}\ x_{-2,1c},\ x_{-2,1s}\ x_{3,1c},\ x_{3,1s}\ x_{-3,1c},\ x_{-3,1s}\ x_{4,1c},\ x_{4,1s}\ x_{-4,1c},\ x_{-4,1s}]$$

The resulting DFI for the vector $\mathbf{x}$ turns out to be $\mathbf{F}_\mathbf{x}$ given by

$$\mathbf{F}_\mathbf{x} = \begin{bmatrix} \alpha_{-4,1} & \alpha_{-3,1} & \alpha_{-2,1} & \alpha_{-1,1} & \alpha_{0,1} & \alpha_{1,1} & \alpha_{2,1} & \alpha_{3,1} & \alpha_{4,1} \\ \alpha^*_{4,0} & \alpha^*_{3,0} & \alpha^*_{2,0} & \alpha^*_{1,0} & \alpha_{0,0} & \alpha_{1,0} & \alpha_{2,0} & \alpha_{3,0} & \alpha_{4,0} \\ \alpha^*_{4,1} & \alpha^*_{3,1} & \alpha^*_{2,1} & \alpha^*_{1,1} & \alpha^*_{0,1} & \alpha^*_{-1,1} & \alpha^*_{-2,1} & \alpha^*_{-3,1} & \alpha^*_{-4,1} \end{bmatrix} \tag{37}$$

B. Hardware setup

An Imperix power test bench was used to test the validity of the EGAM model. The laboratory setup of the system is shown in Fig. 8. A rapid prototyping controller sends the switching modules' gate drive signals via optical channels. The inverter comprises two half-bridge switching modules with Silicon Carbide MOSFETs rated for 800 V and 24 A. Table III presents the parameters of the inverter system test-bed. The components were chosen so that hardware dynamics and mathematical dynamics would coincide without being influenced by the values used to obtain the results.

TABLE III: Inverter system parameters

Input filter inductor, L_1	2.2 mH
Output filter inductor, L_2	2.2 mH
Input filter capacitor, C_1	520 µF
Output filter capacitor, C_2	10 µF
Load resistance, R	45 Ω
Inductor resistance, R_L	87 mΩ
Modulation frequency $\bar{f}$	50 Hz
Switching frequency, $\hat{f}$	10 kHz
Modulation signal phase, $\bar{\phi}$	Dependent on hardware test phase
Carrier signal phase, $\hat{\phi}$	0 rad

TABLE IV: Startup test parameters

Parameter	Value
V_{in}	50 V
Modulation Index	0.75
ω_1 harmonic count	4
ω_2 harmonic count	1

Two tests are performed on the inverter. These are:

1) The Start-up test
2) Modulation index step test

Details are provided for the tests mentioned above in the following two subsections.

C. The Start-up test

Table IV provides the startup test parameters. The input voltage is first given on the dc side. A step enable causes the SPWM signals to be applied to the inverter model. The subsequent dynamics are shown in Fig. 9a - Fig. 9d.

The DFI in the EGAM model accounts for four harmonics on the modulation side and one on the switching side. Therefore, both the dc and ac side harmonics are visible. The dc side is expected to have even order harmonics visible on the dc side. The experimental results show excellent congruence with the results obtained by the EGAM and PLECS models. Thus, the effectiveness of the proposed EGAM model is demonstrated.

D. Modulation step test

Table V shows the modulation step test parameters. After attaining a steady state with an initial value of the modulation index, a step change is applied to it. The subsequent dynamics are presented in Fig. 10a - Fig. 10d. Again, the results obtained with the EGAM model are a very good agreement with those obtained with the PLECS and hardware models.

E. Effect of Harmonic Truncation

Two cases with different levels of harmonic truncation are used to demonstrate the importance of choosing the correct truncation sizes for attaining appropriate modeling accuracy, as explained in Section IV. Switching harmonics are neglected in this test to focus on the modulation signal's performance. The startup test results of the dc side inductor L_1 are shown in Fig. 11 to do a deeper study on harmonic truncation effects.

The dc side inductor current in an inverter is known to have components at twice the modulation frequency. If the harmonics in EGAM are considered for $p = 1, r = 0$, the resulting

This article has been accepted for publication in IEEE Transactions on Power Electronics. This is the author's version which has not been fully edited and content may change prior to final publication. Citation information: DOI 10.1109/TPEL.2023.3276631

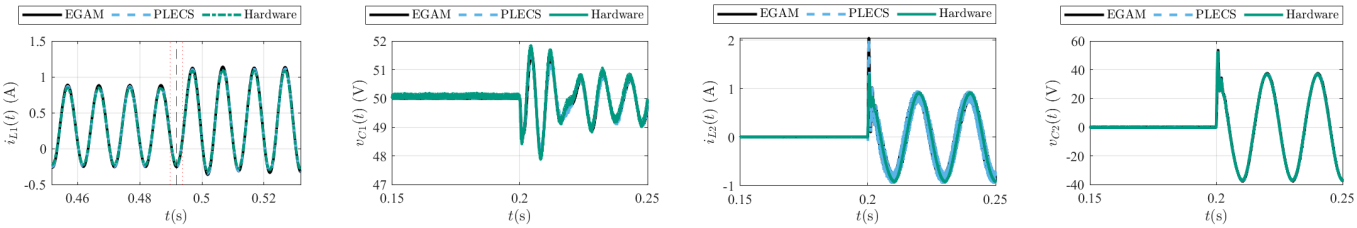

(a) dc side inductor current (b) dc side capacitor voltage (c) ac side inductor current (d) ac side capacitor voltage

Fig. 9: EGAM, PLECS, and hardware comparison results for startup transient test

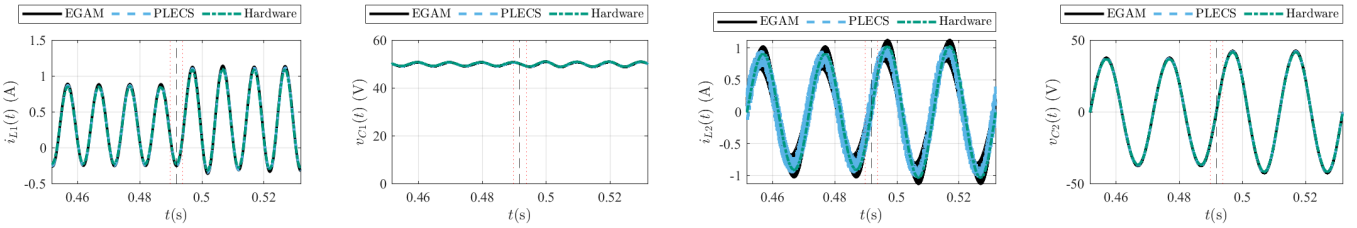

(a) dc side inductor current (b) dc side capacitor voltage (c) ac side inductor current (d) ac side capacitor voltage

Fig. 10: EGAM, PLECS, and hardware comparison results for modulation step transient test

TABLE V: Modulation step test parameters

Parameter	Value
V_{in}	50 V
Modulation index initial	0.75
Modulation index final	0.85
ω_1 harmonic count	4
ω_2 harmonic count	1

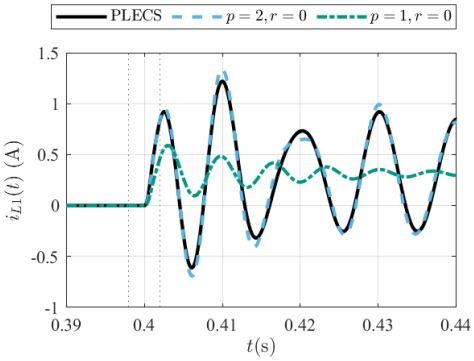

Fig. 11: Harmonic truncation effects on dc inductor current

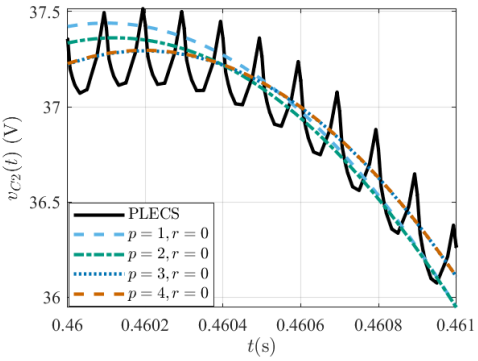

Fig. 12: Modulation harmonics' performance

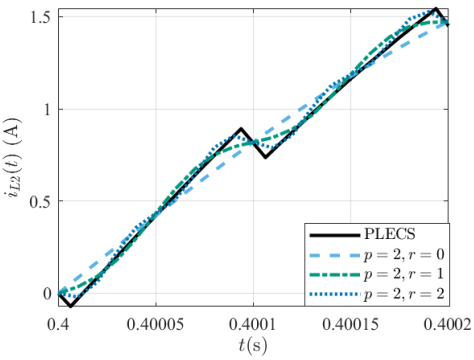

Fig. 13: Switching harmonics' performance

dynamic performance is very poor and does not match the actual PLECS simulation. This poor performance is attributed to harmonic truncation, which leads to the loss of features in the state variable at twice the modulation frequency, thereby underscoring the detrimental effects of harmonic truncation. As the DFI in the EGAM for this case at least has the dc component, the waveform is seen to track the average behavior of the PLECS simulation waveform.

On the other hand, when EGAM is rerun for $p = 2, r = 0$, the harmonic truncation encompasses the components at twice the modulation frequency. The features are preserved in the state variables, thereby making harmonic truncation a good approximation. The same behavior can be shown for the dc side capacitor as well.

TABLE VI: EGAM performance comparison to increase in modulation harmonics

Case	MAE (PLECS vs EGAM)	% improvement over first case
$p=1, r=0$	0.18020	0
$p=2, r=0$	0.17272	4.151
$p=3, r=0$	0.12563	30.285
$p=4, r=0$	0.12570	30.242

TABLE VII: EGAM performance comparison to increase in switching harmonics

Case	MAE (PLECS vs EGAM)	% improvement over first case
$p=2, r=0$	0.15474	0
$p=2, r=1$	0.12660	18.184
$p=2, r=2$	0.11698	24.399

F. Harmonic effects on model accuracy

EGAM increases model accuracy if more harmonics are included. Two examples show an increase in model accuracy as more harmonics are included individually in each axis of the DFI. To compare EGAM simulations analytically, *Mean Absolute Error* (MAE) is computed between PLECS-simulated (baseline) and the EGAM-simulated outputs. MAE is given by

$$\text{MAE} = \frac{\sum_{i=1}^{L} \mid u_i - v_i \mid}{L} \tag{38}$$

where u is the predicted value, v is the baseline value, and L is the length of the window for comparison.

In the first example in Fig. 12, the inverter's ac side filter capacitor's voltage waveform is shown for a snapshot in a steady state where different EGAM models are overlayed on top of the PLECS model. As the modulation signal's harmonics are increased on the p axis, EGAM's accuracy increases. Table VI shows the MAE for different EGAM models and their improvement. As the ac side of the inverter responds more strongly with odd harmonics of the modulation signal, a significant improvement is found in model accuracy for $p=3, r=0$ compared to $p=1, r=0$ case. EGAM for $p \geq 3$ tracks the cycle average of the PLECS waveform more closely.

In the second example shown in Fig. 13, the startup transient of the inverter is shown with emphasis on the switching ripple performance. As r-axis harmonics increase, EGAM matching with PLECS simulation increases. The model for $r=0$ tracks the cycle average of the PLECS simulation due to harmonic truncation, whereas the more complex EGAM simulations exhibit the switching behaviors as well. MAE performance of EGAM compared to PLECS simulation for Fig. 13 is shown in Table. VII

G. Fourier plane plots of harmonic components

EGAM simulations also give insights into how each Fourier coefficient vector in the state variables performs at different frequencies. Fig. 14, and 15 show the time progression of the state variables in the frequency domain for the dc and ac side inductors, respectively. The dc side inductor states are predominantly subjected to even harmonics, so the components x_{10} have negligible values (as noted by the y-axis magnitudes). On the other hand, the AC side components have insignificant values of x_{20} while having significant values of x_{10}.

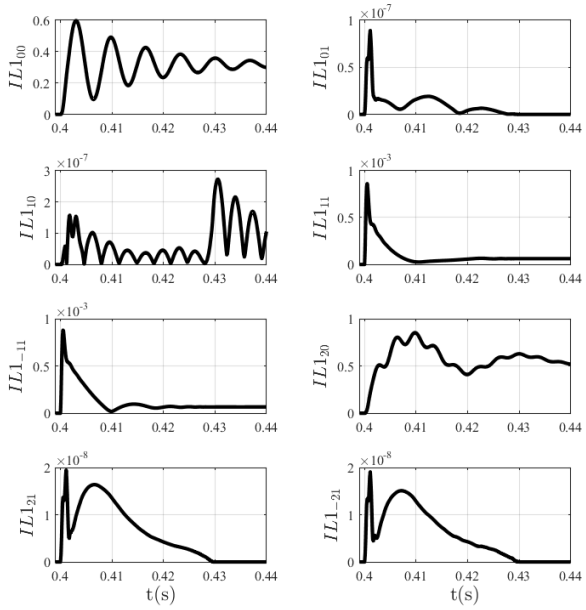

Fig. 14: DC side inductor Fourier plane plots for startup simulation

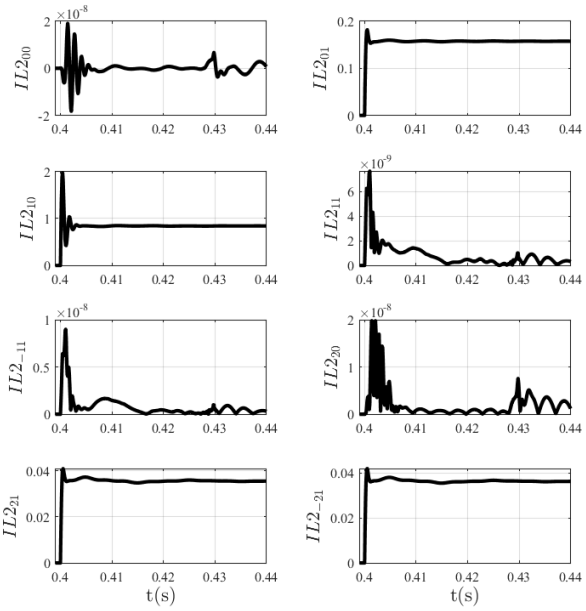

Fig. 15: AC side inductor Fourier plane plots for startup simulation

VI. Conclusion

This article proposes a novel modeling technique to extend the capabilities of the conventional GAM by handling the DFS products using the DFI representation of signals in the

frequency domain. The problem of multiplying two DFS signals is investigated using the proposed theory. Furthermore, an algorithm is proposed to resolve the resulting two-dimensional convolutions for implementation in numerical ODE solvers and is shared as a MATLAB toolbox in Appendix B. To balance mathematical modeling and practicality, a single-phase inverter is used as a test example to show the validity of the proposed method, and an excellent correlation is observed between the detailed model and EGAM. In the future, EGAM can model the dynamics of more complicated systems such as an ac-ac DAB [20]–[22], wherein state variables are subjected to two different frequencies of excitation. Thus, the proposed technique offers a systematic way of easily incorporating many harmonic components in an averaged model to accurately capture the system dynamics at existing and evolving system harmonics. The harmonic truncation phenomenon plays an important role in model accuracy, and its selection was shown using the inverter example. It was also shown that increasing the number of harmonics in the EGAM simulations improved the matching with the detailed simulation model.

APPENDIX A
DFS PRODUCT AND 2D CONVOLUTION

This section provides the proof for Corollary 3.0.2. But before starting with the actual proof for the corollary, some important identities and functions are given for clarity.

A. Preliminary identities

1) An integral identity:

$$\int_{-\pi}^{\pi}\int_{-\pi}^{\pi}\sum_{p,q\ \in\mathbb{Z}}\sum_{r,s\ \in\mathbb{Z}} a_{p,q}b_{r,s}e^{j(k_1\omega_1 t+k_2\omega_2 t)}\ d\omega_1 t\ d\omega_2 t = \begin{cases} 4\pi^2 & k_1=0, k_2=0 \\ 0 & k_1=0, k_2\in\mathbb{Z} \\ 0 & k_1\in\mathbb{Z}, k_2=0 \\ 0 & k_1\in\mathbb{Z}, k_2\in\mathbb{Z} \end{cases} \tag{39}$$

2) Two-dimensional sifting property:

$$x(n_1,n_2)=\sum_{k_1=-\infty}^{\infty}\sum_{k_2=-\infty}^{\infty} x(k_1,k_2)\delta(n_1-k_1,n_2-k_2) \tag{40}$$

3) Multidimensional discrete convolution:

$$x(n_1,n_2,\cdots,n_M)\overset{M}{*\cdots*}h(n_1,n_2,\cdots,n_M)\triangleq \sum_{k_1=-\infty}^{\infty}\sum_{k_2=-\infty}^{\infty}\cdots\sum_{k_M=-\infty}^{\infty} h(k_1,k_2,\cdots,k_M) x(n_1-k_1,n_2-k_2,\cdots,n_M-k_M) \tag{41}$$

4) Double Fourier series signals:

$$x(\omega_1 t,\omega_2 t)=\sum_{j,k\in\mathbb{Z}} a_{j,k}e^{i(m\omega_1 t+n\omega_2 t)} \tag{42}$$

$$y(\omega_1 t,\omega_2 t)=\sum_{j,k\in\mathbb{Z}} b_{j,k}e^{i(m\omega_1 t+n\omega_2 t)} \tag{43}$$

5) Fourier coefficients in 2D:

$$\overline{C}_{mn}=\frac{1}{4\pi^2}\int_{-\pi}^{\pi}\int_{-\pi}^{\pi} f(p,q)\ e^{-j(mp+nq)}\ dp\ dq \tag{44}$$

Proof 1:

$$\begin{aligned}
\overline{C}_{mn} &= \frac{1}{4\pi^2}\int_{-\pi}^{\pi}\int_{-\pi}^{\pi} x(\omega_1 t,\omega_2 t)\ y(\omega_1 t,\omega_2 t)\ e^{-j(m\omega_1 t+n\omega_2 t)}\ d\omega_1 t\ d\omega_2 t \\
&= \frac{1}{4\pi^2}\int_{-\pi}^{\pi}\int_{-\pi}^{\pi}\sum_{p,q\in\mathbb{Z}} a_{p,q}e^{j(p\omega_1 t+q\omega_2 t)} \sum_{r,s\in\mathbb{Z}} b_{r,s}e^{j(r\omega_1 t+s\omega_2 t)}\ \ e^{-j(m\omega_1 t+n\omega_2 t)}\ d\omega_1 t\ d\omega_2 t \\
&= \frac{1}{4\pi^2}\sum_p\sum_q\sum_r\sum_s a_{p,q}b_{r,s} \int_{-\pi}^{\pi}\int_{-\pi}^{\pi} e^{-j((m-p-r)\omega_1 t+(n-q-s)\omega_2 t)}\ d\omega_1 t\ d\omega_2 t \\
&\overset{(39)}{=} \sum_p\sum_q\sum_r\sum_s a_{p,q}b_{r,s}\ \delta((m-p)-r,(n-q)-s) \\
&= \sum_p\sum_q a_{p,q}\sum_r\sum_s b_{r,s}\ \delta((m-p)-r,(n-q)-s) \\
&\overset{(40)}{=} \sum_p\sum_q a_{p,q}b_{m-p,n-q}
\end{aligned}$$

$$\overline{C}_{mn}\overset{(41)}{=} a**b \tag{45}$$

APPENDIX B
EGAM TOOLBOX

A toolbox is developed for MATLAB to perform the EGAM simulations for power converters and is shared as a GitHub project (https://github.com/KartikeyaVeeramraju/EGAMToolbox). The toolbox includes functions for applying the 2D convolution algorithm for ODE solvers.

ACKNOWLEDGMENT

This article has been authored by an employee of National Technology & Engineering Solutions of Sandia, LLC under Contract No. DE-NA0003525 with the U.S. Department of Energy (DOE). The employee owns all right, title and interest in and to the article and is solely responsible for its contents. The United States Government retains and the publisher, by accepting the article for publication, acknowledges that the United States Government retains a non-exclusive, paid-up, irrevocable, world-wide license to publish or reproduce the published form of this article or allow others to do so, for United States Government purposes. The DOE will provide public access to these results of federally sponsored research in accordance with the DOE Public Access Plan https://www.energy.gov/downloads/doe-public-access-plan. Any subjective views or opinions that

might be expressed in the article do not necessarily represent the views of the U.S. Department of Energy or the United States Government. This project was supported in part by the Office of Electricity Energy Storage Program.

REFERENCES

[1] S. Sanders, J. Noworolski, X. Liu, and G. Verghese, "Generalized averaging method for power conversion circuits," *IEEE Transactions on Power Electronics*, vol. 6, no. 2, pp. 251–259, 1991.

[2] V. Caliskan, O. Verghese, and A. Stankovic, "Multifrequency averaging of dc/dc converters," *IEEE Transactions on Power Electronics*, vol. 14, no. 1, pp. 124–133, 1999.

[3] H. Alrajhi, "A generalized state space average model for parallel dc-to-dc converters," *Computer Systems Science and Engineering*, vol. 41, no. 2, pp. 717–734, 2022.

[4] H. Qin and J. W. Kimball, "Generalized average modeling of dual active bridge dc–dc converter," *IEEE Transactions on Power Electronics*, vol. 27, no. 4, pp. 2078–2084, 2012.

[5] M. Monika, M. Rane, S. Wagh, A. Stanković, and N. Singh, "Development of dynamic phasor based higher index model for performance enhancement of dual active bridge," *Electric Power Systems Research*, vol. 168, pp. 305–312, 2019.

[6] G. Brando, A. Del Pizzo, and S. Meo, "Model-reference adaptive control of a dual active bridge dc-dc converter for aircraft applications," in *2018 International Symposium on Power Electronics, Electrical Drives, Automation and Motion (SPEEDAM)*, 2018, pp. 502–506.

[7] M. Berger, I. Kocar, H. Fortin-Blanchette, and C. Lavertu, "Hybrid average modeling of three-phase dual active bridge converters for stability analysis," *IEEE Transactions on Power Delivery*, vol. 33, no. 4, pp. 2020–2029, 2018.

[8] Z. U. Zahid, Z. M. Dalala, C. Zheng, R. Chen, W. E. Faraci, J.-S. J. Lai, G. Lisi, and D. Anderson, "Modeling and control of series–series compensated inductive power transfer system," *IEEE Journal of Emerging and Selected Topics in Power Electronics*, vol. 3, no. 1, pp. 111–123, 2015.

[9] H. Fang, H. Xiang, S. Li, Y. Xin, J. Zhou, and Y. Wang, "Dynamic phasor modeling of mmc-hvdc systems," in *2022 IEEE 5th International Conference on Information Systems and Computer Aided Education (ICISCAE)*, 2022, pp. 988–995.

[10] O. C. Sakinci and J. Beerten, "Generalized dynamic phasor modeling of the mmc for small-signal stability analysis," *IEEE Transactions on Power Delivery*, vol. 34, no. 3, pp. 991–1000, 2019.

[11] A. Francés, R. Asensi, O. García, R. Prieto, and J. Uceda, "Modeling electronic power converters in smart dc microgrids—an overview," *IEEE Transactions on Smart Grid*, vol. 9, no. 6, pp. 6274–6287, 2018.

[12] S. K. Gurumurthy, M. Mirz, B. S. Amevor, F. Ponci, and A. Monti, "Hybrid dynamic phasor modeling approaches for accurate closed-loop simulation of power converters," *IEEE Access*, vol. 10, pp. 101 643–101 655, 2022.

[13] A. Nazari, Y. Xue, J. K. Motwani, I. Cvetkovic, D. Dong, and D. Boroyevich, "Dynamic phasor modeling of three phase voltage source inverters," in *2021 6th IEEE Workshop on the Electronic Grid (eGRID)*, 2021, pp. 1–6.

[14] U. C. Nwaneto and A. M. Knight, "Dynamic phasor-based modeling and simulation of a reduced-order single-phase inverter in voltage-controlled and current-controlled modes," in *2020 IEEE Texas Power and Energy Conference (TPEC)*, 2020, pp. 1–6.

[15] ——, "Dynamic phasor-based modeling and simulation of a single-phase diode-bridge rectifier," *IEEE Transactions on Power Electronics*, vol. 38, no. 4, pp. 4921–4936, 2023.

[16] Z. Shuai, Y. Peng, J. M. Guerrero, Y. Li, and Z. J. Shen, "Transient response analysis of inverter-based microgrids under unbalanced conditions using a dynamic phasor model," *IEEE Transactions on Industrial Electronics*, vol. 66, no. 4, pp. 2868–2879, 2019.

[17] A. Bendib, A. Kherbachi, A. Chouder, H. Ahmed, and K. Kara, "Advanced control scheme and dynamic phasor modelling of grid-tied droop-controlled inverters," *IET Renewable Power Generation*, 2022.

[18] J. Mahdavi, A. Emaadi, M. Bellar, and M. Ehsani, "Analysis of power electronic converters using the generalized state-space averaging approach," *IEEE Transactions on Circuits and Systems I: Fundamental Theory and Applications*, vol. 44, no. 8, pp. 767–770, 1997.

[19] J. A. Mueller and J. W. Kimball, "An improved generalized average model of dc–dc dual active bridge converters," *IEEE Transactions on Power Electronics*, vol. 33, no. 11, pp. 9975–9988, 2018.

[20] K. J. Veeramraju, A. Sharma, and J. W. Kimball, "A comprehensive analysis on complex power flow mechanism in an ac-ac dual active bridge," in *2022 IEEE Power and Energy Conference at Illinois (PECI)*, 2022, pp. 1–6.

[21] A. Sharma, K. J. Veeramraju, and J. W. Kimball, "Power flow control of a single-stage ac-ac solid-state transformer for ac distribution system," in *2022 IEEE Power and Energy Conference at Illinois (PECI)*, 2022, pp. 1–6.

[22] H. Qin and J. W. Kimball, "Solid-state transformer architecture using ac–ac dual-active-bridge converter," *IEEE Transactions on Industrial Electronics*, vol. 60, no. 9, pp. 3720–3730, 2013.

[23] X. Liu, A. M. Cramer, and F. Pan, "Generalized average method for time-invariant modeling of inverters," *IEEE Transactions on Circuits and Systems I: Regular Papers*, vol. 64, no. 3, pp. 740–751, 2017.

[24] X. Liu and A. M. Cramer, "Three-phase inverter modeling using multifrequency averaging with third harmonic injection," in *2016 IEEE Energy Conversion Congress and Exposition (ECCE)*, 2016, pp. 1–6.

[25] S. Sen, P. L. Evans, and C. Mark Johnson, "Multi-frequency averaging (mfa) model of a generic electric vehicle powertrain suitable under variable frequency of averaging developed f or remote operability," *IET Electrical Systems in Transportation*, vol. 10, no. 3, pp. 268–274, 2020.

[26] S. Sen, P. L. Evans, and C. M. Johnson, "Multi-frequency averaging (mfa) model of electric-hybrid powertrain suitable for variable frequency operation applied in geographically-distributed power hardware-in-the-loop (gd-phil) simulation," in *2018 IEEE Vehicle Power and Propulsion Conference (VPPC)*, 2018, pp. 1–6.

[27] A. V. Oppenheim, A. S. Willsky, and S. H. Nawab, *Signals & Systems (2nd Ed.)*. USA: Prentice-Hall, Inc., 1996.

[28] P. Shamsi, "Extended averaging method for power supply systems with multiple switching frequencies," in *2014 IEEE Applied Power Electronics Conference and Exposition - APEC 2014*, 2014, pp. 2842–2846.

[29] X. Liu, "Improvements in inverter modeling and control," Ph.D. dissertation, University of Kentucky, 2017.

[30] K. J. Prasad Veeramraju and J. W. Kimball, "Multidimensional extensions to generalized averaged models for multi-frequency-excited dynamic systems," in *2021 IEEE 22nd Workshop on Control and Modelling of Power Electronics (COMPEL)*, 2021, pp. 1–8.

Kartikeya Jayadurga Prasad Veeramraju (GS'19) earned his B.Tech degree in Electrical and Electronics Engineering from Kakatiya University, India in 2017 and his MS in Electrical Engineering from Missouri University of Science and Technology, Rolla, MO, in 2020. He is currently pursuing his Ph.D. in Power Electronics at the same university. His research interests include the design, modeling, and embedded control of power converters, microgrids, EV chargers, and high-voltage aerospace power converters. He has been a key member of the Missouri S&T satellite team, where he has developed power converters for satellites. Additionally, he worked as a graduate teaching assistant, teaching power systems and electromechanics laboratory courses to undergraduate students while at Missouri S&T.

Jacob A. Mueller (M'18) received the B.S., M.S., and Ph.D. degrees in electrical engineering from Missouri University of Science and Technology, Rolla, MO, in 2012, 2014, and 2018, respectively. He is currently Senior Member of Technical Staff with the Power Electronics and Energy Conversion Systems group at Sandia National Laboratories, Albuquerque, NM. His research interests include modeling and control of power electronics and high-performance power conversion systems for utility applications.

Jonathan W. Kimball (M'96–SM'05) received the B.S. degree in electrical and computer engineering from Carnegie Mellon University, Pittsburgh, PA, USA, in 1994, and the M.S. degree in electrical engineering and the Ph.D. degree in electrical and computer engineering from the University of Illinois at Urbana-Champaign, Champaign, IL, USA, in 1996 and 2007, respectively.

He was with Motorola, Phoenix, AZ, USA, from 1996 to 1998, where he was involved in designing insulated gate bipolar transistor modules for industrial applications. He then joined Baldor Electric, Fort Smith, AR, USA, where he designed industrial adjustable-speed drives ranging 1–150 hp. In 2003, he joined the University of Illinois at Urbana-Champaign, as a Research Engineer, where he then became a Senior Research Engineer. In 2003, he cofounded SmartSpark Energy Systems, Inc., Champaign, where he was the Vice President of Engineering. In 2008, he joined the Missouri University of Science and Technology, Rolla, MO, USA, where he is currently the Fred W. Finley Distinguished Professor of Electrical Engineering, as well as chair of the Department of Electrical and Computer Engineering.

Dr. Kimball is a Member of Eta Kappa Nu, Tau Beta Pi, and Phi Kappa Phi. He is a licensed Professional Engineer in the state of Illinois.